ADVANCED FUNCTIONAL MATERIALS
www.afm-journal.de

Gold Nanoclusters-Based Nanoprobes for Simultaneous Fluorescence Imaging and Targeted Photodynamic Therapy with Superior Penetration and Retention Behavior in Tumors

Chunlei Zhang, Chao Li, Yanlei Liu, Jingpu Zhang, Chenchen Bao, Shujing Liang, Qing Wang, Yao Yang, Hualin Fu, Kan Wang, and Daxiang Cui**

Gold nanoclusters (GNCs) attract increasing attention due to their potential applications in sensing, catalysis, optoelectronics, and biomedicine. Herein, the formation of highly fluorescent glutathione (GSH)-capped GNCs is achieved through the delicate control of the reduction kinetics and thermodynamic selection of the Au(I)–SG complexes. Furthermore, the GNCs-based nanoprobes are developed by the covalent coupling folic acid (FA) and PEG (polyethylene glycol) on the surface of GNCs directly, followed by trapping photosensitizer (chlorin e6, Ce6) within PEG networks and attaching to the GNCs surface. The fabricated nanoprobes (Ce6@GNCs-PEG_{2K}-FA) possess a uniform particle size (hydrodynamic diameter ≈6.1 ± 1.2 nm), without affecting the yield of singlet oxygen of the trapped Ce6. In vitro studies show the enhanced cellular uptake and satisfactory photodynamic therapy (PDT) effectiveness toward MGC-803 cells when compared with free Ce6. The biodistribution and excretion pathway studies of the nanoprobes in MGC-803 tumor-bearing nude mice reveal their superior penetration and retention behavior in tumors, while the preserved features of renal clearance and stealthy to reticulo-endothelial system are mainly attributed to the small hydrodynamic diameters and the FA-capped PEGylated ligands. The enhanced PDT efficacy and the nontoxicity to mice provide an exciting new nano-platform with promising clinical translational potential.

1. Introduction

Over recent decades, great advances have been made in various nano-platforms for cancer diagnosis and therapy, including many nanomatrials with different chemical compositions and physicochemical properties, such as liposomes, polymeric micelles, and inorganic nanoparticles.[1,2] Generally, the nanomaterials-based theranostic agents were developed by a combination of therapy techniques, for example, chemotherapy,[3] radiotherapy,[4,5] and photo-triggered therapy,[6] with various imaging technologies, such as fluorescence imaging, Raman imaging, magnetic resonance imaging, and photoacoustic imaging.[6,7] Compared with small molecular tracers, one of the main advantages of nanoprobes is their passively targeting ability to tumor tissues by enhanced permeability and retention (EPR) effect.[2] However, many inorganic-based theranostic agents, such as carbon-based,[8] metal-based and semiconductor-based nanomaterials,[9,10] have relatively larger hydrodynamic diameters (HDs, typically >10 nm), which are above the of kidney filtration threshold (KFT) of 5.5 nm. Therefore, those nanomaterials prefer to be nonspecifically trapped in liver and spleen by the reticulo-endothelial system (RES) after systematic administration, which not only reduces the tumor targeting efficiency and specificity but also induces the latent toxicity for normal organs, hampering their clinical use.[10,11] Conversely, smaller nanoparticles (NPs) penetrate well into the tumor tissues, but are limited by their rapid systemic elimination. This phenomenon could partially be due to their different diffusion behavior in dense tumor interstitial matrix. The diffusion of NPs larger than 60 nm is often hindered, causing them to accumulate preferentially in perivascular regions and exert only local effects, whereas, smaller NPs (<20 nm) can achieve substantial enhancement in transport across the interstitial and tumor vascular wall, but suffering a fast clearance through renal filtration.[12] However, ideal nanomaterials-based theranostic agents should have little accumulation in normal tissues while getting adequate doses in tumor locations. With the growing appreciation of the great progress in the synthesis of gold nanoclusters (GNCs), in vivo applications of GNCs as theranostic agents are experiencing an upsurge of interest.[13,14]

The current synthetic capabilities allow a wide range of thiolates, proteins, DNA, dendrimers, polypeptides, and their derivatives to tune the surface chemistry of GNCs.[13,15] In

C. Zhang, C. Li, Y. Liu, J. Zhang, C. Bao, S. Liang, Q. Wang, Y. Yang, Dr. H. Fu, Dr. K. Wang, Prof. D. Cui
Institute of Nano Biomedicine and Engineering
Key Laboratory for Thin Film and Microfabrication Technology of the Ministry of Education
Department of Instrument Science and Engineering
School of Electronic Information and Electrical Engineering
Shanghai Jiao Tong University
800 Dongchuan RD
Shanghai 200240, China
E-mail: wk_xa@163.com; dxcui@sjtu.edu.cn

DOI: 10.1002/adfm.201403095

particular, the glutathione (GSH)-capped GNCs (GNCs@GSH) have undergone relatively thorough research with the successful determination of their structures and quantized electronic states.[16] The large Stokes shift, excellent photostability and facile surface functionalization are the attractive features of GNCs@GSH. However, the most reported GNCs@GSH possessed a low quantum yield (QY) and showed a very weak fluorescence, which limited the practical use in bioimaging, sensing and other fields. Recent studies have shown that renal-clearable GNCs behave like small molecules in urinary elimination and two-compartment pharmacokinetics while preserving the EPR effect.[14,17] In addition, GNCs can be retained in the tumor at a higher concentration but cleared from normal tissues >3 times faster than the dye molecules.[18] Compared with traditional small drug, dye molecules and lager nanomaterials with HDs >10 nm, the GNCs-based nanoprobes hold many advantages including: (1) passively targeting to tumors by EPR effect with small amounts trapped in the liver and spleen; (2) a much longer tumor retention time and faster normal tissue clearance; (3) excellent water solubility, good biological compatibility, and the versatility in surface chemistry. These merits enable the GNCs to be a new nano-platform with promising clinical translational potential. Recently, advances in cancer cell and tumor imaging and fluorescent imaging- or X-ray CT imaging-guided chemotherapy and radiotherapy have been made,[5,19] nonetheless, a GNCs-based drug delivery system that has not been developed to transport photosensitizers for simultaneous bioimaging and targeted photodynamic therapy (PDT) in vitro and in vivo.

Herein, the red-emitting GSH-capped GNCs with a QY of 5.8% were synthesized from a modified tetrabutylammonium borohydride (TBAB)-reduction method.[19] TBAB is a mild reducing agent and provides mild and controllable reduction kinetics for the formation of GNCs. Next, the GNCs-based, folic acid (FA)-coupled, and PEG (polyethylene glycol)-functionalized nanoprobes were developed to load the photosensitizer of chlorin e6 (Ce6) molecules (**Scheme 1** and Figure S1, Supporting Information). Incorporation of a flexible PEG spacer between the clusters and FA provides a means of endowing an exterior coat for "stealth" while greatly enhancing cell surface recognition. Systematic in vitro and in vivo experiments are designed to carefully evaluate the cellular uptake, light-induced cell apoptosis, biodistribution, as well as FA-directed active tumor targeting and enhanced PDT at the animal level. Different from the previously reported gold nanoparticles (GNPs)-based photosensitizer delivery system,[20] our GNCs-based nanoprobes (Ce6@GNCs-PEG$_{2K}$-FA) with well-engineered surface chemistry enable superior penetration and long retention behavior in tumors, signals from tumor site are distinctly detectable up to 7 days. More importantly, rapid diffusion followed by effective elimination from normal tissues renders the nanoprobes as a multifunctional promising theranostic agent with specificity, efficacy, and safety.

2. Results and Discussion

2.1. Preparation and Characterization of GNCs and GNCs-Based Nanoprobes

GNCs were synthesized from a modified TBAB-reduction method (see the Experimental Section).[19,21] Our

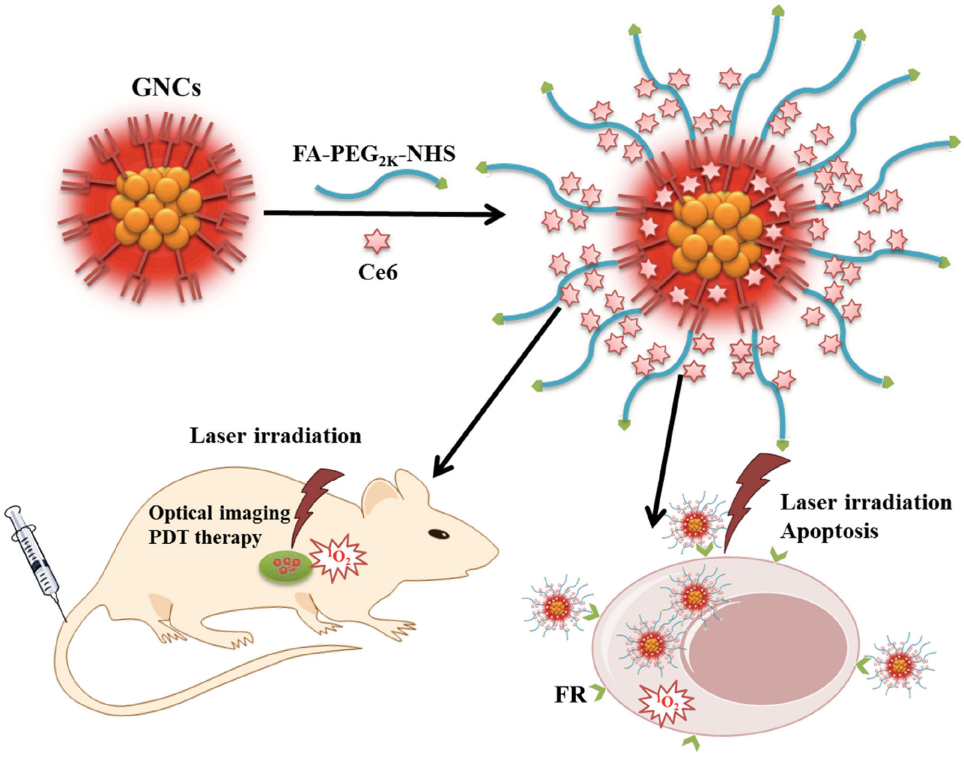

Scheme 1. Schematic illustration of the preparation of the GNCs-based nanoprobes and their applications in vitro and in vivo.

TBAB-reduction method conducted under ice bath realized the delicate control of the reduction kinetics and thermodynamic selection of the Au(0)@Au(I)–SG structures. The committed step in the formation of highly fluorescent GNCs was the reduction of insoluble large Au(I)–SG complexes to soluble oligomeric Au(I)–SG complexes and then Au(0)@Au(I)–SG structure with the addition of TBAB. Slower thermodynamic aging step allows a dense aggregation of Au(0)@Au(I)–SG intermediates according to the theoretical studies of aggregation-induced emission (AIE) discovered by Xie et al.[22] As shown in **Figure 1**a,b, transmission electron microscopy (TEM) and high-resolution TEM (HRTEM) images indicated that the monodispersed GNCs exhibit spherical shape and outstanding size uniformity with a diameter of 2.0 ± 0.3 nm. The final product of GNCs was brownish in aqueous solution and emitted intensive red light under UV illumination (insets in Figure 1c). No surface plasmon absorption was observed in the UV–vis spectrum of the as-synthesized GNCs, which was different from the conventional larger plasmonic-nanoparticles. This is mainly attributed to the large amount of Au(I) atoms in the GNCs, resulting in the failure to denote free electrons to support surface plasmons.[14] The photoluminescence (PL) spectrum showed a main peak at 652 nm with a shoulder peak at ≈820 nm. Meanwhile, the photoluminescence excitation (PLE) spectrum showed a main excitation peak at 520 nm, which correspond well to the absorption peak of 515 nm in the absorption spectrum (Figure 1c). The high content of Au(I)–SG complexes in the GNCs was confirmed by X-ray photoelectron spectroscopy (XPS) measurement, which showed that ≈43.0% of Au atoms in the GNCs were actually in the Au(I) state, forming strong Au(I)–S bonds with the GSH ligands (Figure 1d). The quantum yield of the as-synthesized GNCs was 5.8% at room temperature, using Rhodamine 6G as the reference.

The nanoprobes of GNCs-PEG_{2K}-FA were prepared by covalent coupling FA-PEG_{2K}-NHS on the surface of GNCs directly, followed by trapping drugs (Ce6) within PEG_{2K} networks and attaching to the GNCs surface. The Ce6 molecules can be stabilized via hydrophobic interactions of PEG_{2K} chains and nonpolar moiety of Ce6, while the terminal three ionizable carboxylic groups (–COO–) of Ce6 molecules might form stable adsorption with Au atoms in physiological pH range (pH 6.5–8.5).[23] The loading content of Ce6 in GNCs-PEG_{2K}-FA determined by UV–vis spectroscopy was ≈6 wt%. The absorption spectra of GNCs-PEG_{2K}-FA, Ce6@GNCs-PEG_{2K}-FA, and pure GNCs and free Ce6 in aqueous solution at pH 7 were shown in **Figure 2**a. Specifically, the spectra of GNCs-PEG_{2K}-FA and Ce6@GNCs-PEG_{2K}-FA, exhibited the characteristic absorption peak of FA with a narrow peak at 283 nm

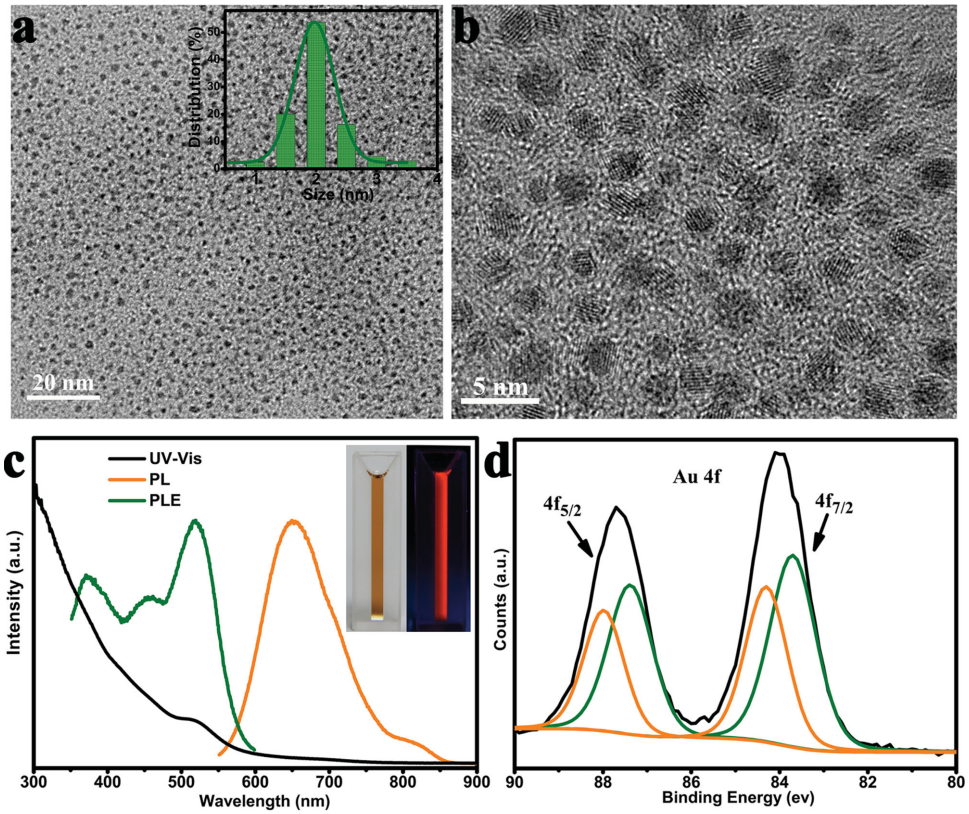

Figure 1. Characterization of red-emitting GNCs. a) TEM and b) HRTEM images of GNCs. (Inset) Core size of GNCs measured by TEM. c) UV–vis absorption (black line), PL (orange line, λ_{ex} = 520 nm), and PLE (olive line, λ_{em} = 652 nm) spectra of GNCs. (Insets) Digital pictures of the GNCs dissolved in water under white-light (left) and UV (365 nm) excitation (right). d) XPS spectrum of GNCs (black line) showing that the Au $4f_{7/2}$ and Au $4f_{5/2}$ binding energies (BE) are 83.9 and 87.6 eV, respectively. With BE of Au $4f_{7/2}$ as an example, the Au $4f_{7/2}$ spectrum of GNCs (black lines) was deconvoluted into Au(I) (orange line) and Au(0) (olive line) components with binding energies of 84.3 and 83.7 eV, respectively. By comparing the integrated areas of two fitting peaks, the Au(I) amount in Au atoms was calculated to be 42.8%.

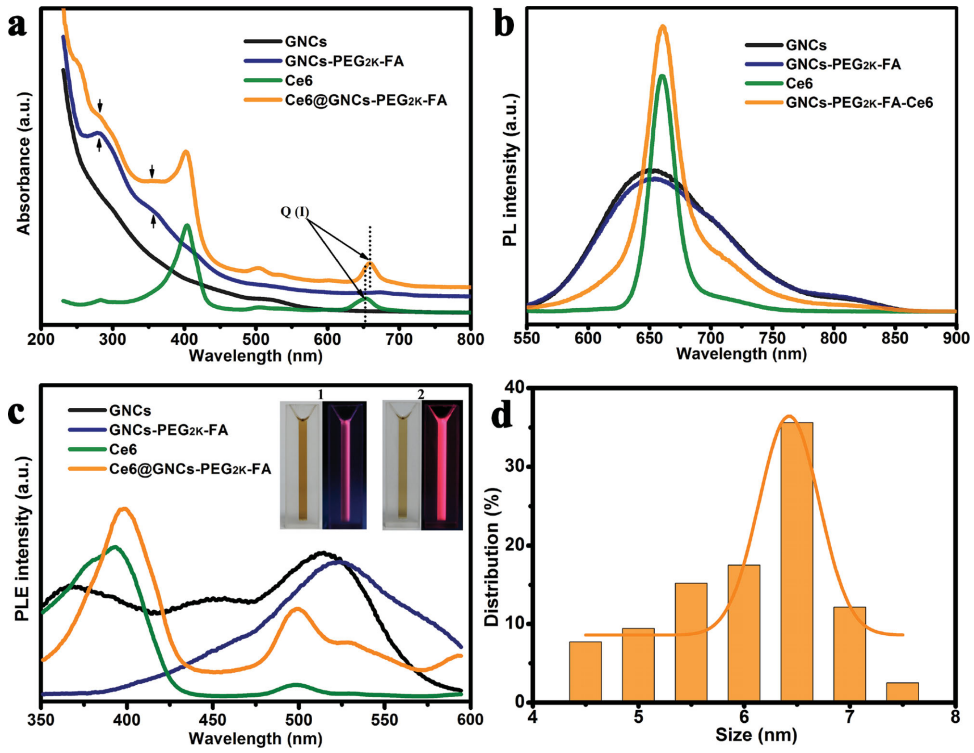

Figure 2. Characterization of the GNCs-based nanoprobes. a) UV–vis absorption, b) PL, and c) PLE spectra of the as-synthesized GNCs (black line, λ_{ex} = 520 nm for PL spectrum, and λ_{em} = 652 nm for PLE spectrum), GNCs-PEG_{2K}-FA (blue line, λ_{ex} = 524 nm for PL spectrum, and λ_{em} = 652 nm for PLE spectrum), free Ce6 (olive line, λ_{ex} = 400 nm for PL spectrum, and λ_{em} = 660 nm for PLE spectrum), and Ce6@GNCs-PEG_{2K}-FA (orange line, λ_{ex} = 500 nm for PL spectrum, and λ_{em} = 660 nm for PLE spectrum). (Insets) Digital pictures of (1) GNCs-PEG_{2K}-FA and (2) Ce6@GNCs-PEG_{2K}-FA dissolved in 1×PBS under white-light (left) and UV (365 nm) excitation (right). d) Hydrodynamic diameter of the nanoprobes (Ce6@GNCs-PEG_{2K}-FA).

and a broad peak at 350 nm.[24] Most pronounced change of the obtained nanoprobes was observed in the region of Ce6 Q(I) band, which underwent a bathochromic shift to 659 nm comparison of the absorption of free Ce6 (654 nm). It was concluded that the generated bathochromic shift of the Q(I) band was a typical response to the changes of the Ce6 environment.[25] In all, the UV–vis spectra indicated the immobilization of FA, PEG_{2K}, and Ce6 on the GNCs, which was further supported by FTIR and ^{1}H NMR spectral measurements (Figures S2,3, Supporting Information). FTIR spectra confirmed the conjugation of PEG_{2K} to the GNCs through the appearance of vibration frequencies at 1647 cm^{-1} (amide C=O) and 1533 cm^{-1} (N–H bond). The peaks at 2870 and 948 cm^{-1} belong to the stretching vibration of the functional group of the $–CH_2–$ of the PEG_{2K} and the peak 1109 cm^{-1} is due to the C–O–C stretch. Besides, the new peak at 1606 cm^{-1}, which is a typical vibration of amino group in the pteridine ring of FA, confirmed successful conjugation of GNCs and PEG_{2K} with FA (Figure S2, Supporting Information). As shown in Figure S3 (Supporting Information), the intensive signal at 3.65 ppm was attributed to PEG blocks ($–CH_2–$). The peculiar signals at 7.65, 8.65, and 2.52 ppm were characteristic signals of the pterin ring, benzene ring, and methylene of FA,[26] respectively, while the chemical shifts from 3.31–3.53 ppm was the striking feature of PEG blocks ($–CH_2–$), suggesting the successful conjugation of FA to the H_2N-PEG_{2K}-COOH. The ^{1}H NMR spectrum of GNCs-PEG_{2K}-FA showed successful covalent attachment of FA-PEG_{2K}-NHS to GNCs through the superimposition of the characteristic chemical shifts of FA-PEG_{2K}-NHS and GNCs. We also noticed that the releasing of Ce6 from GNCs-PEG_{2K}-FA was pH-dependent and showed increased leaking under acid pH (Figure S4, Supporting Information), indicating that the protonation of carboxyl groups was helpful for Ce6 releasing.

For the PL spectra, GNCs-PEG_{2K}-FA showed no appreciable change in fluorescence intensity when excited at 520 nm, while the fluorescence intensity of Ce6@GNCs-PEG_{2K}-FA did not display a simple superposition of GNCs and Ce6 at corresponding concentrations of both components (Figure 2b). The excitation of Ce6 in the nanoprobes was triggered partly by energy transfer from the excited GNCs, since the PLE intensity of the hybrid nanoprobes was lower than pure GNCs when excited at 520 nm as demonstrated in the PLE spectra (Figure 2c). Both GNCs-PEG_{2K}-FA and Ce6@GNCs-PEG_{2K}-FA displayed bright red emission under UV irradiation (insets in Figure 2c). The average hydrodynamic diameter of the resulting nanoprobes (Ce6@GNCs-PEG_{2K}-FA) measured by DLS was 6.1 ± 1.2 nm (Figure 2d), which could be contributed to the extended hydration layer thickness by the polymer chain of PEG. In addition, analysis of the XPS spectrum determined ≈42.8% Au(I) component of all Au atoms in the resulting nanoprobes, indicating the unchanged structures of GNCs (Figure S5, Supporting Information).

2.2. Cellular Uptake Assay

The targeting effectiveness of the FA ligands in the nanoprobes toward gastric cancer MGC-803 cells (over-expression of folate receptor (FR)) was evaluated by the confocal laser scanning microscopy (CLSM) and flow cytometry (FCM). The MGC-803 cells were treated with Ce6@GNCs-PEG_{2K}-FA and free Ce6 at the equivalent concentrations of Ce6 and the fluorescence was monitored over a period of 12 h. As shown in **Figure 3**a, only dim red fluorescence was detected in the cells incubated with free Ce6 for 0.5 h, suggesting the low quantity of Ce6 that has entered the cells. In contrast, bright fluorescence was distributed in the cytoplasm and cytomembrane after the cells have been incubated with Ce6@GNCs-PEG_{2K}-FA for 0.5 h. The median fluorescence values revealed by FCM also confirmed the higher fluorescence intensity of the cells incubated with the nanoprobes, which was 1.2-fold higher than that of the cells incubated with free Ce6 (Figure 3b). The most significant difference in the amount of cellular uptake between Ce6@GNCs-PEG_{2K}-FA and free Ce6 occurred after 3 h of incubation with a 4.8-fold higher median fluorescence value. The endo/lysosomal organelles in MGC-803 cells were stained by LysoTracker Green DND-26. As a result, both free Ce6 and the nanoprobes were mainly distributed in endo/lysosomal compartments following internalization. Recent investigations in our previous study and others have confirmed the low cellular affinity of free GNCs, which was mainly attributable to the surface zwitterionization under physiological pH range.[19,27] To further evaluate the targeting recognition capability of the GNCs-based nanoprobes, GES-1 cells (human gastric epithelial cells; FR-negative) incubated with free Ce6 and Ce6@GNCs-PEG_{2K}-FA was assessed as a control experiment. As shown in Figure S6 (Supporting Information), free Ce6 distributed in the cytomembrane and cytoplasm of GES-1 cells while the fluorescence intensity increased greatly along the incubation time of 3–12 h. The GES-1 cells incubated with Ce6@GNCs-PEG_{2K}-FA displayed dim red fluorescence even after 12 h incubation. ICP-MS (inductively coupled plasma mass spectrometry) method was also employed to quantify the intracellular Au content in MGC-803 and GES-1 cells after 12 h of GNCs-PEG_{2K}-FA or GNCs incubation. It was found that the GNCs-PEG_{2K}-FA exhibited an approximately 10.3-fold higher cellular uptake than GNCs in MGC-803 cells (Figure S7, Supporting Information). Overall, these observations demonstrated the introduction of the FA ligands could significantly improve the specific targeting properties of the nanoprobes toward FR overexpressed MGC-803 cancer cells while preserving little accession to the normal cells.

2.3. In Vitro Cellular Toxicity

The excited photosensitizer interacts with molecular oxygen and results in the production of ROS (reactive oxygen species), especially singlet oxygen ($^1O_2$), which can lead to the damage of cellular constituents and subsequent cell death.[28] First, singlet oxygen detection test using a singlet oxygen sensor

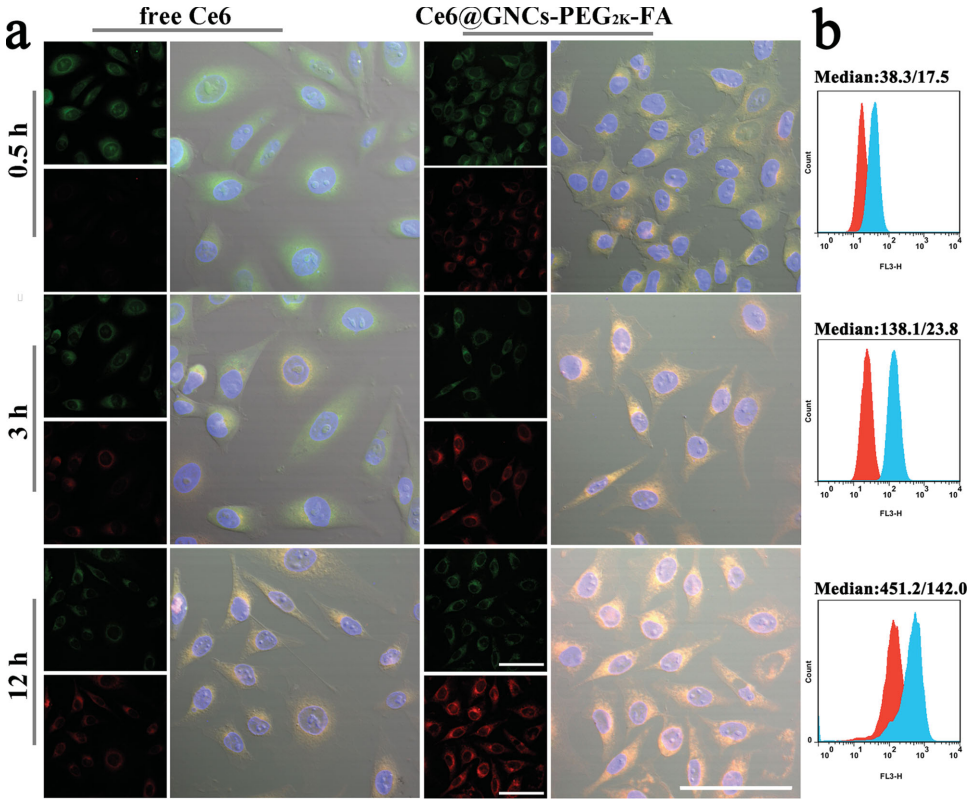

Figure 3. a) Confocal images of MGC-803 cells exposured to free Ce6 and Ce6@GNCs-PEG_{2K}-FA for 0.5, 3, and 12 h. b) Flow cytometry analysis of cellular uptake, red and cyan histograms represent the cellular uptake of free Ce6 and Ce6@GNCs-PEG_{2K}-FA, respectively.

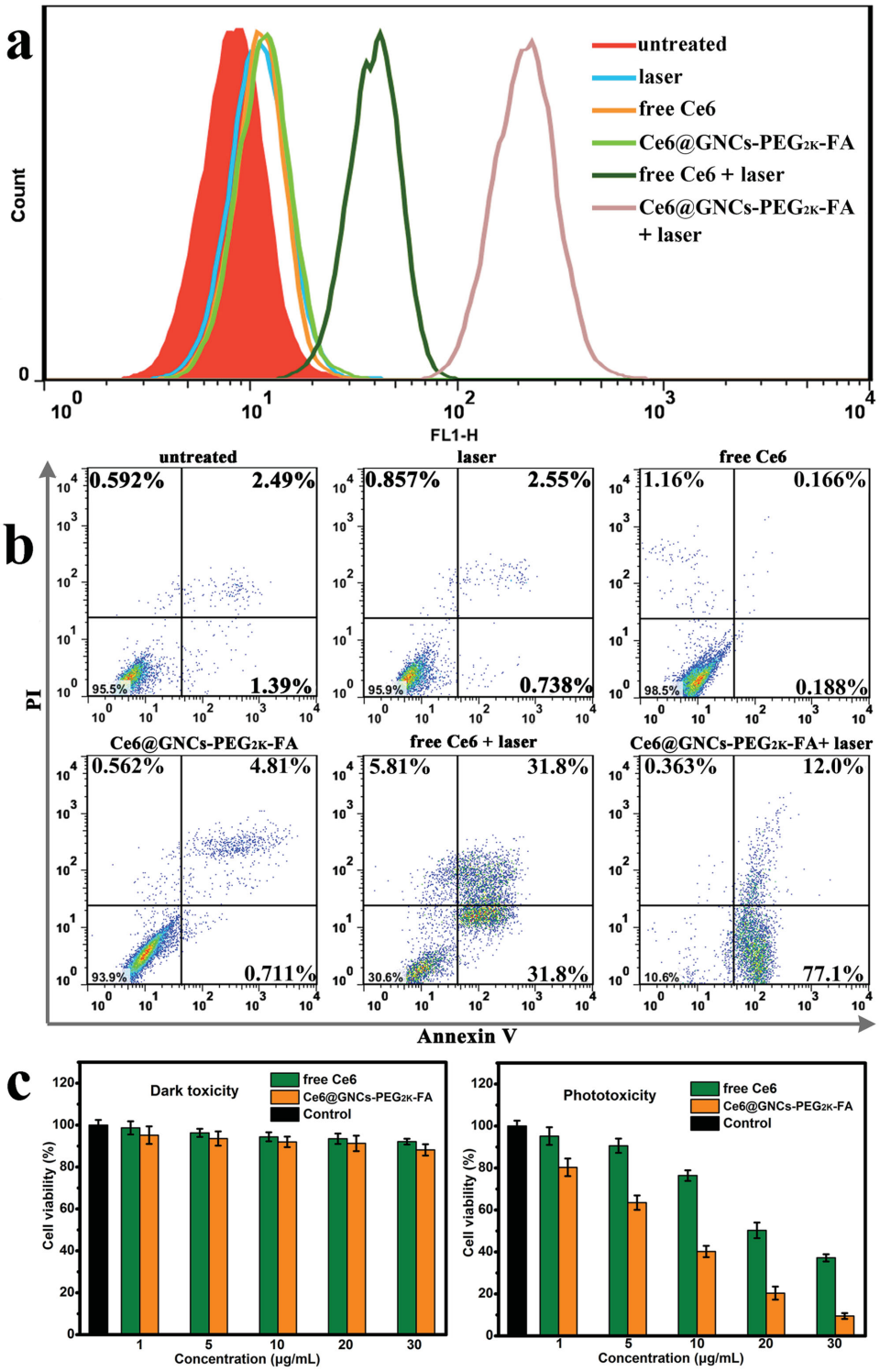

Figure 4. a) Flow cytometric detection of ROS generation in the presence of DCFH-DA. b) Flow cytometric analysis of MGC-803 cell death induced by PDT of free Ce6 or Ce6@GNCs-PEG$_{2K}$-FA. c) Dark toxicity and photocytoxicity of free Ce6 and Ce6@GNCs-PEG$_{2K}$-FA toward MGC-803 cells, analyzed by MTT assay.

green (SOSG) reagent exhibited that Ce6@GNCs-PEG$_{2K}$-FA had almost the same capability to produce singlet oxygen as free Ce6 (Figure S8, Supporting Information). Therefore, we examined the intracellular ROS production by free Ce6 and the nanoprobes in MGC-803 cells via DCFH-DA staining method. As anticipated, the nanoprobes induced the most amounts of ROS under irradiation, which was detected with flow cytometry (**Figure 4**a). Next, the photocytotoxicity of the nanoprobes

and free Ce6 in the presence of 633 nm laser irradiation was evaluated by MTT assay and apoptosis assay with Annexin V-FITC and propidium iodide (PI) double staining. Apoptosis is responsible for PDT-mediated cell death in certain cell lines.[28,29] To clarify the mechanism of cell death induced by the nanoprobes under laser irradiation, we examined both early and late apoptotic cells using flow cytometry (Figure 4b). It was found that minimal apoptosis and necrosis were observed in the cells (with a cell mortality <7%) exposed to either the nanoprobes or free Ce6 in the dark or cells with only laser exposure. However, under the same laser exposure, MGC-803 cells in the presence of 30 μg mL^{-1} free Ce6 induced significantly apoptosis with 31.8% for early apoptosis and 31.8% for late apoptosis. By comparison, cells exposured to the nanoprobes demonstrated a considerably enhanced fraction of apoptosis (77.1% and 12.0% for early and late apoptosis, respectively). As shown in Figure 4c, quantitative MTT assay indicated the low dark toxicity of the nanoprobes, whereas, the cells treated with the nanoprobes exhibited about 2-fold to 3-fold higher cell death ratios than that treated with free Ce6 upon laser irradiation, suggesting superior photocytoxicity of the nanoprobes over free Ce6. The increased proportions of cell death in the nanoprobes treated cells could be attributed to the increased cellular uptake, and subsequently more ROS production. The Ce6 loaded nanoprobes have shown excellent biocompatibility as well as good photocytoxicity upon irradiation, suggesting the great potentials of the GNCs-based nanoprobes as powerful photosensitizer for PDT treatment.

2.4. Tumor-Targeting Evaluation of the Nanoprobes

The encouraging results from the in vitro performance promoted the in vivo evaluation. The pharmacokinetic parameters of the GNCs-based nanoprobes (lacking drugs) were first measured in BALB/c mice following systemic administration. In the circulation, GNCs-PEG_{2K}-FA followed a two-compartment pharmacokinetics with a distribution half-life ($t_{1/2\alpha}$) and elimination half-life ($t_{1/2\beta}$) values of 0.17 ± 0.013 and 20.49 ± 1.87 h, respectively (Figure S9, Supporting Information). The shorter distribution half-life could be attributed to its small HDs and the longer elimination half-life could be achieved by the prolonged circulation attributed to PEGylation. The two-compartment model is critical for ensuring the successful implementation of rapidly achieving and long tumor retention. Next, the biodistribution and excretion pathway, along with the targeted delivery efficiency and PDT effect of the nanoprobes were investigated with small animal fluorescence imaging, elemental gold analysis, and histological examination in a series of time points. The tumor targeting capability of the nanoprobes was investigated by injecting the nanoprobes (Ce6@GNCs-PEG_{2K}-FA) intravenously into the mice, and monitoring the in situ fluorescence images of MGC-803 tumor-bearing nude mice. In a proof-of-concept study, we primarily compared the passive tumor targeting effectiveness of free Ce6, GNCs, and BSA-directed synthesis of gold nanoclusters (GNCs@BSA). As shown in Figures S10–12 (Supporting Information), free Ce6 had the relatively shorter tumor retention time less than 24 h, which was a specific pharmacokinetic feature of small dye molecules; whereas GNCs@BSA exhibited relatively higher liver accumulation and GNCs had the highest tumor targeting efficiency. For the GNCs-based nanoprobes, significant fluorescence (700/30 nm) was observed at the tumor site just minutes after intravenous injection (**Figure 5**a). With time growing, the decrease in the fluorescence background from normal tissues accompanied by the increased accumulation in the tumors caused the tumor areas to become increasingly apparent at 3 h post injection (p.i.). The fluorescence signals collected from tumor areas reached maximum at 8 h p.i., and this signal maintained its intensity without significantly changed within 24 h. Moreover, ex vivo fluorescence imaging of the nanoprobes in tumor, heart, liver, spleen, lung, brain, bladder, and kidney at 10 min, 1, 24, 48, and 72 h, and 7 days p.i. provided additional insights into the tumor targeting efficiency and clearance pathways (Figure 5b). The fluorescence signals from tumor regions and the corresponding 3D surface plots suggested the homogeneous distribution of the nanoprobes throughout the whole tumor tissues at 1, 24, and 48 h p.i., while the strong fluorescence signals from bladder at 1 h and 24 h p.i. indicated that the GNCs-based nanoprobes retained the efficient renal filtration and urinary excretion of GNCs. In contrast, the weak signals from livers and spleens have convincingly ruled out the nonspecific accumulation in the reticuloendothelial system.

Furthermore, the accumulation of the nanoprobes in tumors and major organs was quantified by identifying the tumors and organs as regions of interest (ROIs) to measure the average fluorescence intensity of 685 to 715 nm (Figure 5c). In addition, we carried out quantitative gold element analysis of collected tissues 24 h p.i. by means of ICP-MS. The distribution of gold content showed a similar proportion with the average fluorescence intensities between different organs, indicating the high stability of the nanoprobes in vivo (Figure S13, Supporting Information). As shown in Figure 5b,c, >75% of the maximum average fluorescence intensity from the nanoprobes remained in the tumor 72 h p.i., and the fluorescence signal was still clearly legible even after 7 days intravenous administration. Therefore, the GNCs-based nanoprobes could allow the Ce6 to maintain relatively superior penetration and retention in tumors than free Ce6, which was further studied by microscopic analysis of the red fluorescence (>590 nm) in tissue cryosections. As expected, similar to the ex vivo tumor images, the red fluorescence observed from the tissue slices of nanoprobes-treated mouse was significantly higher than those treated with free Ce6 or GNCs (Figure 5d). These findings supported the design rationale of the nanoprobes, where selectively accumulation and prolonged retention of drugs in the tumor tissues with higher concentrations can be achieved through the combination of active and passive targeting abilities. More importantly, these results also implied the distribution and diffusion of the drugs in the nanoprobes were mainly influenced by the FA-mediated active tumor targeting and then FR-mediated endocytosis.[30] Moreover, we observed that all of the organs exhibited an overall decrease in Au content at 7 days p.i. (Figure S14, Supporting Information). The tumor showed moderate decrease in Au content, while the nanoprobes were removed from cardio-pulmonary (heart, lung) significantly and the remained could redistributed or channeled into the metabolic and excretory organs (liver, kidney) where the ultrasmall

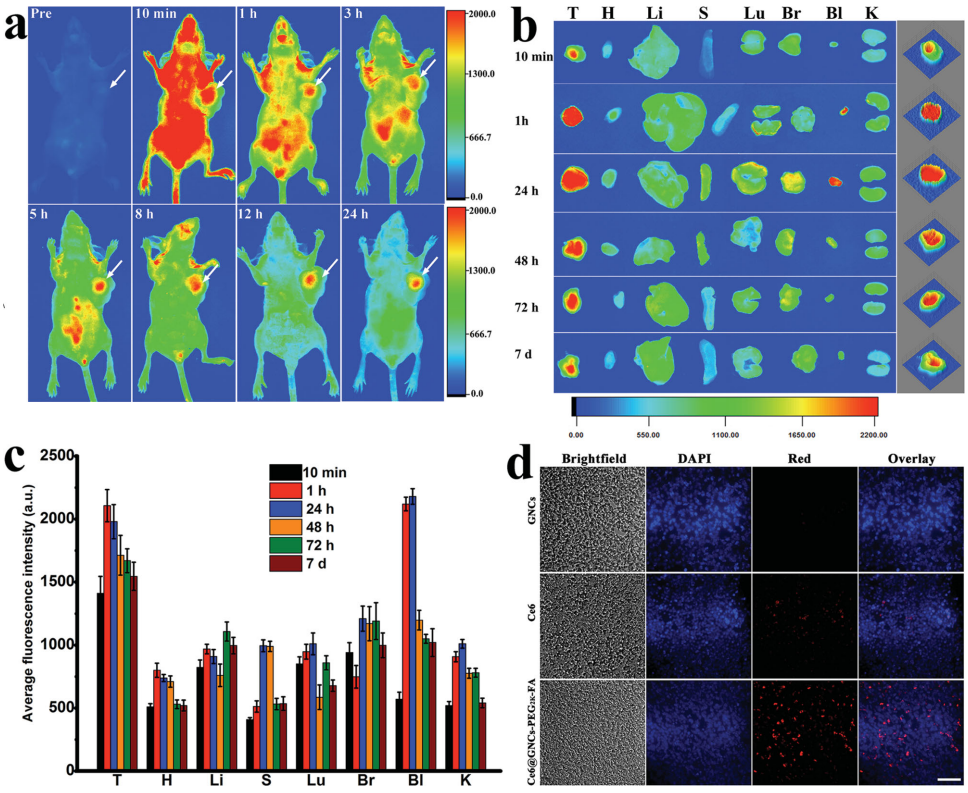

Figure 5. a) In vivo fluorescence imaging of MGC-803 tumor-bearing mouse after intravenous injection of Ce6@GNCs-PEG_{2K}-FA over a period of 24 h. b) Representative ex vivo fluorescence images of major organs and tumors of mice after different post-injection times. T (tumor), H (heart), Li (liver), S (spleen), Lu (lung), Br (brain), Bl (bladder), K (kidney). The right columns were the corresponding 3D surface plot images of pixel intensities obtained from the tumor regions using NIH Image J software. c) Quantitative biodistribution of Ce6@GNCs-PEG_{2K}-FA in different organs and tumors based on ROIs analysis of the average fluorescence intensity from the tumors and normal tissues (3 mice per group). d) Representative fluorescence images of tumor cryosections (10 μm). Images presented are bright-field, blue fluorescence (DAPI), red fluorescence (>590 nm), and merged (overlap) images. Scale bar, 100 μm.

nanoprobes could be finally cleared out of the body through kidney filtration and excretion in the form of feces.

2.5. In Vivo PDT Performance on MGC-803 Tumor-Bearing Mice

Efficient delivery of Ce6 into the cancer cells of solid tumor by the nanoprobes increased the intracellular drug concentration, ultimately leading the cell death under laser irradiation. We further evaluated the therapeutic efficacy of the nanoprobes-induced PDT treatment in vivo and the changes in tumor volumes were monitored over 21 days. As shown in **Figure 6**a, the PDT efficiency increased by the following order: PBS ≈ free Ce6 ≈ Ce6@GNCs-PEG_{2K}-FA < free Ce6 with laser irradiation <Ce6@GNCs-PEG_{2K}-FA with laser irradiation. The GNCs-based nanoprobes exhibited the most superior in vivo PDT performance, which mainly result from a combination of the EPR effect of nanoscale probes and the active targeting capability provided by the FA molecules. We also performed TUNEL (terminal deoxynucleotidyl transferase-mediated-dUTP nick-end labeling) assay to assess the proportions of the apoptotic cells in tumor tissues. TUNEL-positive tumor cells (exhibit bright green fluorescence) were detected in tumor tissues of the mice treated with Ce6@GNCs-PEG_{2K}-FA and laser irradiation, whereas apoptotic cells were comparatively fewer or rarely detectable in other groups (Figure 6b). These results suggested that the laser irradiation was essential to generate singlet oxygen to cause the apoptosis of tumor cells and then the destruction of the tumor tissues. Potential in vivo toxicity is always a great concern in the applications of nanomaterials-based drug delivery system. Hematoxylin and eosin (H&E) stained slices of heart, liver, spleen, lung, kidney, and brain indicated no apparent abnormality or lesion after 21 days post-treatment of Ce6@GNCs-PEG_{2K}-FA (Figure 6c). The blood biochemistry after 1 day and 7 days of intravenously injection was analyzed to further evaluate the effect of the GNCs-based nanoprobes on in vivo toxicity. Since exogenous substances are mainly metabolized and cleared through liver and kidney, we focused specifically on the biomarkers that represented potential acute toxicity in liver and kidney. The levels of alkaline phosphatase (ALP), total bilirubin (TBIL), alanine transaminase (ALT), aspartate aminotransferase (AST), gamma glutamyl transferase (GGT), and lactate dehydrogenase (LDH) were determined, which are important indicators of liver function. Also, we analyzed the levels of blood urea nitrogen (BUN), creatinine (CREA), and uric acid (UA), which are important indicators of kidney function. As shown in Figure S15 (Supporting Information), there were no significant toxicity symptoms were observed between the GNC-based

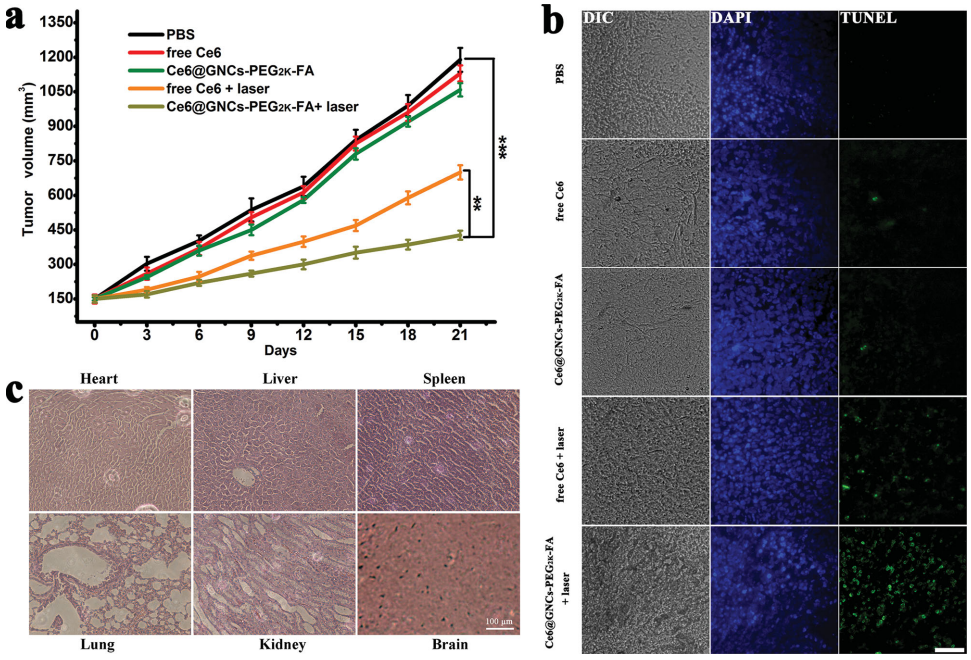

Figure 6. a) Tumor growth of mice in different treatment groups within 21 days. Data are represented as mean ± SD (5 mice per group), $^{**}p < 0.005$, $^{***}p < 0.001$. b) TUNEL staining of tumor sections from different groups. Green color represents positive TUNEL staining and blue color is from DAPI, a dye for staining nuclei. c) H&E stained tissue sections from the heart, liver, spleen, lung, kidney, and brain of the mouse after 21 days post-treatment of Ce6@GNCs-PEG_{2K}-FA. Scale bar, 100 μm.

nanoprobes-treated mice and their normal control group. This was consistent with the pathology results that there was no injury in the structure of all organs.

3. Conclusions

In summary, by covalent bond formation and noncovalent hydrophobic interactions, we have developed a novel GNCs-based Ce6 delivery nano-platform to achieve selective targeting toward cancer cells and tumors combining PDT therapy. For the nanoprobes, the Ce6, trapped on the GNCs and PEG networks, has shown more efficient and rapid release within hours different from that of free Ce6 without a GNCs-based drug vector. The origin of the resulted biodistribution and efficient tumor targeting was mainly attributed to the small hydrodynamic diameters and the FA-capped PEGylated ligands of the nanoprobes, which were remaining renal clearable and stealthy to RES organs. Over the 7 days study period, rapid accumulation within 10 min and longtime retention and superior penetration behavior light one path to the applications of GNCs as a clinically translational platform.

4. Experimental Section

Materials: Tetrabutylammonium borohydride (TBAB; 95%), Triethylamine (TEA), *N*,*N*′-dicyclohexylcarbodiimide (DCC), and *N*-hydroxysuccinimide (NHS) were obtained from Aladdin Reagent Co. Ltd. (Shanghai, China). Gold(III) chloride trihydrate ($HAuCl_4 \cdot 3H_2O$, 99%), folic acid (FA), anhydrous dimethyl sulfoxide (DMSO), and tetrahydrofuran were obtained from Sinopharm Chemical Reagent Co., Ltd. (Shanghai, China). Amine-PEG-carboxyl (H_2N-PEG-COOH, MW ≈ 2K) was purchased from Laysan Bio, Inc. (Huntsville, AL, USA). Sephadex G-25 and G-100 were purchased from Pharmacia (Uppsala, Sweden). Amicon Ultra Centrifugal Filter devices were purchased from Millipore Corporation. Annexin V-FITC/PI Apoptosis Detection Kit and TUNEL Kit containing FITC-labelled dUTP were purchased from Yeasen Corporation (Shanghai, China). 4′,6-diamidino-2-phenylindole (DAPI), LysoTracker Green DND-26, 2′,7′-dichlorofluorescein diacetate (DCFH-DA), and 3-[4,5-dimethylthiazol-2-yl]-2,5-diphenyltetrazolium bromide (MTT) were purchased from Invitrogen Corporation (Carlsbad, CA, USA). Chlorin e6 (Ce6) was obtained from Frontier Scientific (Utah, USA). MGC-803 cells and GES-1 cells were available in the Cell Bank of Type Culture Collection of Chinese Academy of Sciences. Cell culture products and reagent, unless mentioned otherwise, were purchased from GIBCO. All the above chemicals were used without any further purification. Ultrapure water (18.2 MΩ cm, Millipore Co., USA) was used in all the preparations.

Synthesis of Red-Emitting GNCs: In a typical synthesis, freshly prepared $HAuCl_4$ (2.5 mL, 20×10^{-3} M) and GSH (1 mL, 150×10^{-3} M) were added to a 50-mL conical flask containing 43.5 mL of cold ultrapure water. The reaction mixture was then cooled down to 0 °C (using an ice bath) and stirring for 3 min, and subsequently cold TBAB solution (TBAB-to-Au ration = 9.3:1, 3 mL) was added and then stirred quickly for 5 min. The reaction solution was incubated in ice bath without stirring for 2 h then the pH of the solution was brought to ≈3.0 by the addition of 1 M HCl. When the pH of the reaction mixture was brought to ≈3.0, free and polydispersed Au(I)–SG complexes had almost zero charge which would automatically be inclined to formation of insoluble Au(I)–thiolate complex aggregates because of their stronger aurophilic Au(I)···Au(I) interactions and reduced electrostatic repulsion. The reaction solution was then aged for 12 h in ice bath. An aqueous solution of strong red-emitting GNCs was formed. The raw red-emitting product was collected after removing the precipitates of Au(I)–SG complexes by centrifugation. The supernatant was further concentrated to 10 mL by a centrifugal filter device (Amicon Ultra-15, MWCO: 3.0 kDa, Millipore Corporation, MA).

The product was precipitated by the addition of NaCl (to 10×10^{-3} M) and cold tetrahydrofuran (to 50%) and collected in a swing rotor at 4500 rpm for 3 min. The collected product was dialyzed against ultrapure water for two days using a dialysis bag (MWCO: 3.5 kDa). The final product was lyophilized and stored at 4 °C until use.

Synthesis of NHS-Activated FA-Conjugated PEG (FA-PEG$_{2K}$-NHS): First, NHS-activated FA (FA-NHS) was prepared following the known procedure.[31] In brief, FA (1 g) was dissolved in 40 mL of anhydrous DMSO containing 0.5 mL of TEA at 40 °C with stirring. To the resulting solution, NHS (0.52 g) and DCC (0.50 g) were added successively, and the reaction mixture was stirred in the dark at room temperature for 18 h. The insoluble byproduct (dicyclohexylurea) was removed by filtration of the reaction mixture through a glass wool plug. The filtrate (i.e., the FA-NHS solution) was precipitate by addition of 3× volume of ice cold 30% acetone/70% diethylether. The FA-NHS was washed three times with acetone/diethylether by resuspending the product and then collecting it by centrifugation. The collected pellet was dried by vacuum freeze-drying. Second, FA-PEG$_{2K}$ was prepared. A typical reaction was as follows: 50 mg of PEG (Amine-PEG-carboxyl, MW ≈ 2000) was dissolved in 20 mL of DMSO. A total of 5 times FA-NHS (62.5 mg) was then dissolved in 10 mL of DMSO. Then FA-NHS was added to the PEG solution followed by stirring for 48 h at room temperature in the dark. The product was isolated from a similar precipitation procedure as last step, and then purified by gelfiltration over a Sephadex G-25 column equilibrated with 0.1 M $NaHCO_3$ (pH 8.3) to remove unconjugated folic acid. After another desalting step over a similar column, the product was lyophilized, yielding the FA–PEG conjugate (FA-PEG$_{2K}$-COOH) as a pale yellow solid. Third, NHS-activated PEG$_{2K}$-FA was prepared with DCC/NHS/TEA (molar ratio described above) in DMSO and FA-PEG$_{2K}$-NHS was purified by precipitation in ice cold ethyl ether and acetone.

Conjugating FA-PEG$_{2K}$-NHS to GNCs and Drug Loading: The amine groups from GNCs (from GSH) could readily be conjugated to the activated esters of FA-PEG$_{2K}$-NHS via a common amine coupling method, thereby finalizing the preparation of GNCs-PEG$_{2K}$-FA nanoprobes. The FA-PEG$_{2K}$-NHS product (40 mg) and GNCs (10 mg) were dissolved in 10 mL of 100×10^{-3} M bicarbonate buffer (pH 8.4). After stirring overnight at room temperature, the reaction solution was concentrated with Amicon Ultra Centrifugal Filters (MWCO 3 kDa; Millipore) and then separated by a Sephadex G-100 column with 0.01 M PBS as eluent. The brown GNCs-PEG$_{2K}$-FA fraction was eluted out prior to the light yellow FA-PEG$_{2K}$-NHS and the brown GNCs. The final product, GNCs-PEG$_{2K}$-FA, was then purified by dialysis (MWCO 14 kDa) against deionized water for 48 h and lyophilization. The FA-PFG$_{2K}$ and its derivatives were characterized using ^{1}H NMR and infrared spectrum analysis. For the Ce6 loaded nanoprobes (Ce6@GNCs-PEG$_{2K}$-FA), 2.5 mg Ce6 in 1 mL of 0.1 M $NaHCO_3$ (pH 8.3) was mixed with 10 mg GNCs-PEG$_{2K}$-FA in 5 mL of 0.1 M $NaHCO_3$ and stirred at room temperature overnight. The nanoprobes were separated by dialysis (MW 3500) against 0.1 M $NaHCO_3$ for 24 h, where the bath solution was changed every 4 h, and then against ultrapure water for 2 days. The nanoprobes were isolated by lyophilization. The Ce6 loading content was determined by dissolving the drug-loaded conjugates and measuring the absorption at 404 nm with a molar extinction coefficient of 1.1×10^5 M^{-1} cm^{-1} after subtracting the absorbance contributed by GNCs-PEG$_{2K}$-FA at the same wavelength. The drug loading content was calculated based on the following equation:[32]

$$\text{Drug loading (\%)} = (\text{weight of drug loaded} / \text{weight of drug loaded and weight of carriers}) \times 100\% \quad (1)$$

The release of Ce6 from Ce6@GNCs-PEG$_{2K}$-FA was studied at 37 °C in two different PBS buffers with pH of 5.0 and 7.4, respectively. In brief, the Ce6@GNCs-PEG$_{2K}$-FA solution (2 mL, 20 mg mL^{-1}) was transferred into a dialysis membrane (MWCO 3500) and immersed into 50 mL of the corresponding buffers with continuously shaken (200 rpm) at 37 °C. At predetermined time intervals, 2 mL aliquots of release media was removed for UV–vis measurement and replenished with an equal volume of fresh media.

Characterization: The size and morphology of the GNCs were characterized by TEM on a JEM-2100F (JEOL, Japan). PL and PLE spectra of GNCs, free Ce6, GNCs-PEG$_{2K}$-FA, and Ce6@GNCs-PEG$_{2K}$-FA were recorded on a Hitachi FL-4600 spectrofluorometer. UV–vis spectra of GNCs, free Ce6, GNCs-PEG$_{2K}$-FA, and Ce6@GNCs-PEG$_{2K}$-FA were measured with a Varian Cary 50 spectrophotometer (Varian Inc., Palo Alto, CA, USA). DLS (dynamic light scattering) measurements were completed using a NICOMP 380 ZLS Zeta Potential/Particle sizer (PSS Nicomp, Santa Barbara, CA, USA). XPS spectra were measured using a Kratos Axis Ultra^{DLD} spectrometer (AXIS Ultra, Kratos Analytical Ltd, Japan). FTIR spectra were taken on a Nicolet 6700 spectrometer (Thermo Electron Corporation, Madison, WI, USA) using KBr pellets. ^{1}H NMR spectra were acquired using a Bruker Avance-III-HD 600 MHz NMR Spectrometer (Bruker BioSpin Corp., Billerica, MA, USA).

Cell Culture and MTT Assay: The MGC-803 and GES-1 cells were maintained at 37 °C (5% CO_2) in Dulbecco's Modified Eagle's Medium (DMEM, HyClone) supplemented with 10% (vol/vol) fetal bovine serum (Gibco), 100 U mL^{-1} penicillin and 0.1 mg mL^{-1} streptomycin. MTT assay was carried out to investigate the dark toxicity and phototoxicity of free Ce6 and the nanoprobes (Ce6@GNCs-PEG$_{2K}$-FA). In brief, MGC-803 cells were seeded in 96-well plate at a density of 5×10^3 cells per well and cultured overnight. The cells were incubated with 100 μL complete medium containing serial concentrations of free Ce6 (1—30 μg mL^{-1}) and Ce6@GNCs-PEG$_{2K}$-FA (equivalent Ce6 1–30 μg mL^{-1}) for 24 h. After washing with 1×PBS and medium replacement, one plate was kept in the dark for studying dark toxicity, and another plate was irradiated using a 633 nm helium-neon (He–Ne) laser at a power of 100 mW cm^{-2} for 60 s. Afterward, the cells under light irradiation were grown for another 12 h. Then the dark toxicity and phototoxicity studies were evaluated by a standard MTT assay. The cell viability was calculated according to the equation: Cell viability = ($OD_{570\ nm}$ of the experimental group/$OD_{570\ nm}$ of the control group) × 100% and the cell viability of control group was denoted as 100%.

Cellular Uptake Assay: For confocal microscopy experiments, MGC-803 and GES-1 cells were plated on 14 mm glass coverslips and allowed to adhere for 24 h. After coincubation with 12 μg mL^{-1} free Ce6, and the GNCs-based nanoprobes (Ce6@GNCs-PEG$_{2K}$-FA) (equivalent Ce6 12 μg mL^{-1}) for different times, the cells were washed twice with PBS sufficiently and fixed with 4% paraformaldehyde. The nuclei of the cells were stained with 4′,6-diamidino-2-phenylindole (DAPI, Invitrogen) for 5 min. We also examined the colocalization of free Ce6, the nanoprobes and lysosome in MGC-803 cells. After incubation, MGC-803 cells were stained with LysoTracker Green DND-26 (200 nM) for 0.5 h and then fixed with 4% paraformaldehyde. Confocal fluorescence imaging studies were performed with a Leica TCS SP8 confocal laser scanning microscopy. DAPI was excited using the blue diode 405 nm laser and emission was recorded between 440 and 470 nm. LysoTracker Green was excited at 488 nm with an argon ion laser, and the emission was collected from 510 to 555 nm. The red fluorescence was excited at 543 nm with an argon ion laser, and the emission was collected from 630 to 680 nm. For flow cytometry (BD FACSCalibur) measurements, MGC-803 cells (1.0×10^5 cells per well in 6-well plates) were cultured in medium for 24 h, and coincubated with free Ce6 or the GNCs-based nanoprobes (Ce6@GNCs-PEG$_{2K}$-FA) (with the same concentrations for confocal fluorescence imaging studies) for different times. After coincubation, the cells were washed with PBS twice to remove the free Ce6 or the nanoprobes, and then the cells were trypsinized and resuspended in 1 mL of PBS for flow cytometry measurements. FL-3 (λ_{em} = 650–700 nm) channel was selected to collect the fluorescence signal of MGC-803 cells. For ICP-MS measurements, MGC-803 and GES-1 cells were treated with GNCs-PEG$_{2K}$-FA and GNCs for 12 h with the same concentration of Au (0.25 mg mL^{-1}). The collected cells were digested with aqua regia (1 part HNO_3 and 3 parts HCl) and the Au content in the cells was measured by inductively coupled plasma mass spectrometer Agilent 7500a (Agilent Technologies, USA).

Singlet Oxygen Detection: The singlet oxygen sensor green (SOSG) regent, which was highly selective for $^1O_2$, was employed here for the detection experiment.[5] Typically, SOSG under the concentration of

2.5×10^{-6} M was introduced to measure the $^1O_2$ generation of free Ce6 (10×10^{-6} M) and the nanoprobes (equivalent Ce6 10×10^{-6} M) under light irradiation at 633 nm (50 mW cm^{-2}). Control groups include SOSG alone, and GNCs-PEG$_{2K}$-FA without Ce6 loading. The generated singlet oxygen was determined by measuring recovered SOSG fluorescence (excitation = 494 nm).

Cellular ROS Detection During Irradiation: After the MGC-803 cells were incubated with free Ce6 (10×10^{-6} M) or Ce6@GNCs-PEG$_{2K}$-FA (equivalent Ce6 10×10^{-6} M) for 24 h in six-well plate, they were further incubated with 20×10^{-6} M DCFH-DA for 20 min and irradiated using a 633 nm He–Ne laser at a power of 100 mW cm^{-2} for 60 s. The cells incubated with free Ce6, Ce6@GNCs-PEG$_{2K}$-FA, and medium only were denoted as control groups. The intracellular ROS generation was measured by staining all the cells with DCFH-DA. Subsequently, the fluorescence intensity of DCF inside the cells was detected by flow cytometer, which was proportional to the amount of ROS produced.

Apoptosis Assay: The apoptotic and necrotic cell distribution were determined by Annexin V-FITC/PI Apoptosis Detection Kit (Yeasen, Shanghai) according to the manufacturer's protocol. In brief, MGC-803 cells were seeded in 6-well plates at 1.0×10^5 cells/well for 24 h before exposure to free Ce6 or the GNCs-based nanoprobes (Ce6@GNCs-PEG$_{2K}$-FA) (with the concentrations for MTT assay). Following 24 h incubation, the cells were washed twice with 1×PBS and the medium was replaced with complete culture medium, followed by an exposure to a 633 nm He–Ne laser at a power of 100 mW cm^{-2} for 60 s. The control cells were maintained in the dark. Afterward, the cells were trypsinized, harvested, washed with 1×PBS and resuspended in 200 µL of binding buffer containing 5 µL Annexin V and 10 µL PI. After incubation in dark at room temperature for 15 min, 400 µL of binding buffer was added to each sample, and the cells were immediately analyzed by BD FACSCalibur (BD Biosciences, Mountain View, CA). The data analysis was performed with FlowJo 7.6 software. Positioning of quadrants on Annexin V/PI plots was performed to distinguish living cells (Annexin V$^-$/PI$^-$), early apoptotic cells (Annexin V$^+$/PI$^-$), late apoptotic cells (Annexin V$^+$/PI$^+$), and necrotic cells (Annexin V$^-$/PI$^+$).

Pharmacokinetics of the GNCs-Based Nanoprobes: The pharmacokinetics of GNCs-based nanoprobes was investigated in BALB/c female mice through intravenous injection of Ce6@GNCs-PEG$_{2K}$-FA (100 µL, equivalent GNCs 20 mg mL^{-1}) by quantitative determination of gold in serum. 200 µL of blood was obtained by retro-orbital vein puncture at 20 min, 1, 6, 12, 24, and 48 h and quantified using ICP-MS method. Serum gold concentration–time profiles were analyzed by PKSolver 2.0 software (China Pharmaceutical University, Nanjing, China) and it was the best to fit into two-compartment model.

In Vivo and Ex Vivo Fluorescence Imaging: All animal experiments were carried out in compliance with the Institutional Animal Care and Use Committee of Shanghai Jiao Tong University. Female BALB/c-nude mice (18–22 g) were obtained from Shanghai Slac Laboratoty Animal Co. Ltd (Shanghai, China). To establish the tumor-bearing mice, MGC-803 cells were resuspended in PBS and 2×10^6 cells/site was subcutaneously injected in the right flank of the mice. The tumors were allowed to develop ≈3 weeks to reach a size of ≈150–200 mm^3 before the biodistribution and imaging studies. GNCs (200 µL, 20 mg mL^{-1}), free Ce6, and Ce6@GNCs-PEG$_{2K}$-FA in 1×PBS solution (at a dosage of 2 mg Ce6/kg of total mouse body weight) were intravenously injected into the tumor-bearing mice. Time-course fluorescent images (excitation: 510/20 nm; emission: 700/30 nm; integration time: 10 s) were acquired on a Bruker In-Vivo F PRO imaging system (Billerica, MA, USA). All the post injection images were captured at the same parameter settings and then scaled to the maximum values. For the ex vivo imaging, the mice were sacrificed, tumors and major organs were collected at 10 min, 1, 24, 48, 72 h, and 7 days post injection. Excised tumor and organs were imaged by the Bruker In-Vivo F PRO imaging system with the same parameters as mentioned above. Bruker Molecular Imaging Software 7.1 Version was used to gain quantitative information in terms of average fluorescence intensity by creating regions of interest (ROIs) around tumors and other organs. For the tumor penetration studies, the mice were sacrificed 24 h p.i. and the tumor tissues were embedded in OCT compound (Tissue-Tek) and frozen sections (10 µm) obtained for further fluorescence microscope (IX 71, Olympus) analysis.

The Biodistribution of BSA-Directed Synthesis of GNCs (GNCs@BSA): The BSA (albumin bovine serum)-directed synthesis of gold nanoclusters was modified according to a previous method.[13] First, freshly prepared $HAuCl_4$ solution (5 mL, 10×10^{-3} M) was added to BSA solution (5 mL, 50 mg mL^{-1}) under vigorous stirring at 37 °C. NaOH solution (0.5 mL, 1 M) was introduced 2 min later, and the mixture was allowed to proceed under vigorous stirring at 37 °C for 24 h. Finally, the GNCs@BSA was lyophilized and stored at 4 °C until use. To assess the biodistribution of GNCs@BSA, the MGC-803 tumor-bearing mice were sacrificed at 24 h after intravenous injection of GNCs@BSA (200 µL, 80 mg mL^{-1}). The organ samples were washed with 1×PBS, dried briefly with filter paper and imaged with similar acquisition parameters (excitation: 510/20 nm; emission: 700/30 nm; integration time: 30 s) mentioned above.

Biodistribution Studies of Ce6@GNCs-PEG$_{2K}$–FA: To evaluate tissue distributions of the GNCs-based nanoprobes, the MGC-803 tumor bearing mice were intravenously injected with Ce6@GNCs-PEG$_{2K}$-FA (200 µL, equivalent GNCs 20 mg mL^{-1}) and sacrificed at 24 h and 7 days post injection. The organ samples were imaged with the same acquisition parameters (excitation: 510/20 nm; emission: 700/30 nm; integration time: 10 s) of in vivo fluorescence imaging. After the quantitative analysis of fluorescence intensity of different organs, they were weighted and the concentrations of gold were measured by the ICP-MS method. For the quantitative gold element analysis, the samples were digested in aqua regia at boiling temperature. The solution was evaporated to 1 mL and subsequently diluted to 10 mL with deionized water. The Au content determination was conducted on an Agilent 7500a and every data point was expressed as a mean ± SD from triplicate samples.

In Vivo PDT: In vivo photodynamic therapy assay was performed using MGC-803 tumor-bearing mice. When the tumor size reached ≈150 mm^3, the mice were randomized into five groups of 5 animals per group and intravenously administrated every three days for 21 days with: (1) PBS (200 µL); (2) free Ce6 (4 mg kg^{-1}) without laser irradiation; (3) Ce6@GNCs-PEG$_{2K}$-FA (equivalent Ce6 4 mg kg^{-1}) without laser irradiation; (4) free Ce6 (4 mg kg^{-1}) with laser irradiation; (5) Ce6@GNCs-PEG$_{2K}$-FA (equivalent Ce6 4 mg kg^{-1}) with laser irradiation. For the irradiated groups, a 633 nm He–Ne laser (100 mW cm^{-2}, 10 min) was used after 8 and 24 h of intravenous injection. The tumor size was measured by a caliper every three days after treatment. The tumor volumes were calculated by using the formula: $V_{tumor} = a \times (b)^2 \times 1/2$, where *a* and *b* represent the maximum length and the minimal width of tumors, respectively. At day 21, the tumors were harvested and the tumor tissues were embedded in OCT compound (Tissue-Tek) and frozen sections (10 µm) obtained for further TUNEL apoptosis staining. The tumor sections were stained with the TUNEL Kit (Yeasen Corporation, Shanghai, China) according to the manufacturer's protocol. The stained tumor slides were observed by fluorescence microscope (IX 71, Olympus).

Histochemical Analysis and Biochemistry Test of the Blood: After the tumor growth monitoring experiments at day 21, mice treated with the nanoprobes (Ce6@GNCs-PEG$_{2K}$-FA) were sacrificed. Heart, liver, spleen, lung, kidney, and brain were removed and then fixed in 4% neutral buffered formalin for at least 1 day. The samples were then dehydrated in an ethanol series, processed into paraffin, and sectioned. Then, H&E (hematoxylin and eosin) staining was carried out in accordance with the standard protocol to monitor the morphological features of each organ. For blood analysis, 200 µL of blood was collected from the BALB/c female mice after intravenous injection of Ce6@GNCs-PEG$_{2K}$-FA (100 µL, equivalent GNCs 20 mg mL^{-1}) 1 day and 7 days. The blood was separated by centrifugation and analyzed by standard biochemical examination.

Statistical Analysis: All data were expressed as mean ± SD (standard error) of at least five independent experiments unless otherwise specified. Statistical analysis was performed by the Student's *t*-test. $^*p < 0.05$ was indicated to be statistical significant.

Supporting Information

Supporting Information is available from the Wiley Online Library or from the author.

Acknowledgements

This work is supported by National Key Basic Research Program (973 Project) (Project No. 2010CB933901), National Natural Scientific Foundation of China (Grant Nos. 81225010, 81028009, and 31170961), 863 project of China (Project No. 2012AA022703 and 2014AA020700), and Shanghai Science and Technology Fund (13NM1401500).

Received: September 8, 2014
Revised: November 28, 2014
Published online: January 16, 2015

[1] a) P. Tanner, P. Baumann, R. Enea, O. Onaca, C. Palivan, W. Meier, *Acc. Chem. Res.* **2011**, *44*, 1039; b) V. P. Torchilin, *Nat. Rev. Drug Discovery* **2005**, *4*, 145; c) Y. Cheng, J. D. Meyers, A.-M. Broome, M. E. Kenney, J. P. Basilion, C. Burda, *J. Am. Chem. Soc.* **2011**, *133*, 2583; d) C. Bao, J. Conde, E. Polo, P. del Pino, M. Moros, P. V. Baptista, V. Grazu, D. Cui, J. M. de la Fuente, *Nanomedicine* **2014**, *9*, 2353.

[2] M. Wang, M. Thanou, *Pharmacol. Res.* **2010**, *62*, 90.

[3] H. L. Wong, R. Bendayan, A. M. Rauth, Y. Li, X. Y. Wu, *Adv. Drug Delivery Rev.* **2007**, *59*, 491.

[4] Z. Chunlei, H. Peng, B. Le, H. Meng, L. Teng, G. Guo, C. Daxiang, *J. Nanosci. Nanotechnol.* **2011**, *11*, 9528.

[5] X.-D. Zhang, Z. Luo, J. Chen, X. Shen, S. Song, Y. Sun, S. Fan, F. Fan, D. T. Leong, J. Xie, *Adv.Mater.* **2014**, *26*, 4565.

[6] Y. Choi, S. Kim, M.-H. Choi, S.-R. Ryoo, J. Park, D.-H. Min, B.-S. Kim, *Adv. Funct. Mater.* **2014**, *24*, 5781.

[7] a) J. Yu, C. Yang, J. Li, Y. Ding, L. Zhang, M. Z. Yousaf, J. Lin, R. Pang, L. Wei, L. Xu, F. Sheng, C. Li, G. Li, L. Zhao, Y. Hou, *Adv. Mater.* **2014**, *26*, 4114; b) C. L. Zavaleta, B. R. Smith, I. Walton, W. Doering, G. Davis, B. Shojaei, M. J. Natan, S. S. Gambhir, *Proc. Natl. Acad. Sci. USA* **2009**, *106*, 13511; c) J. Lin, S. Wang, P. Huang, Z. Wang, S. Chen, G. Niu, W. Li, J. He, D. Cui, G. Lu, *ACS Nano* **2013**, *7*, 5320.

[8] Z. Liu, K. Chen, C. Davis, S. Sherlock, Q. Cao, X. Chen, H. Dai, *Cancer Res.* **2008**, *68*, 6652.

[9] X. Michalet, F. F. Pinaud, L. A. Bentolila, J. M. Tsay, S. Doose, J. J. Li, G. Sundaresan, A. M. Wu, S. S. Gambhir, S. Weiss, *Science* **2005**, *307*, 538.

[10] S. K. Balasubramanian, J. Jittiwat, J. Manikandan, C.-N. Ong, L. E. Yu, W.-Y. Ong, *Biomaterials* **2010**, *31*, 2034.

[11] D. Peer, J. M. Karp, S. Hong, O. C. FaroKhzad, R. Margalit, R. Langer, *Nat. Nanotechnol.* **2007**, *2*, 751.

[12] a) S. Huo, H. Ma, K. Huang, J. Liu, T. Wei, S. Jin, J. Zhang, S. He, X. J. Liang, *Cancer Res.* **2013**, *73*, 319; b) S. Sunoqrot, J. Bugno, D. Lantvit, J. E. Burdette, S. Hong, *J. Controlled Release* **2014**, *191*, 115.

[13] J. Xie, Y. Zheng, J. Y. Ying, *J. Am. Chem. Soc.* **2009**, *131*, 888.

[14] Z. Chen, H. Guiyang, P. Thomas, L. Jinbin, Y. Mengxiao, S. Shasha, O. K. Oz, S. Xiankai, Z. Jie, *Angew. Chem., Int. Ed.* **2012**, *51*, 10118.

[15] a) R. Jin, *Nanoscale* **2010**, *2*, 343; b) F. Grohn, B. J. Bauer, Y. A. Akpalu, C. L. Jackson, E. J. Amis, *Macromolecules* **2000**, *33*, 6042.

[16] A. Mathew, T. Pradeep, *Part. Part. Syst. Charact.* **2014**, *31*, 1017.

[17] Z. Chen, M. Long, Q. Yanping, S. Xiankai, Z. Jie, *Angew. Chem., Int. Ed.* **2011**, *50*, 3168.

[18] J. Liu, M. Yu, C. Zhou, S. Yang, X. Ning, J. Zheng, *J. Am. Chem. Soc.* **2013**, *135*, 4978.

[19] C. Zhang, Z. Zhou, Q. Qian, G. Gao, C. Li, L. Feng, Q. Wang, D. Cui, *J. Phys. Chem. B* **2013**, *1*, 5045.

[20] a) Y. Cheng, A. C. Samia, J. Li, M. E. Kenney, A. Resnick, C. Burda, *Langmuir* **2010**, *26*, 2248; b) D. C. Hone, P. I. Walker, R. Evans-Gowing, S. FitzGerald, A. Beeby, I. Chambrier, M. J. Cook, D. A. Russell, *Langmuir* **2002**, *18*, 2985; c) K. Hari, A. Pichaimani, P. Kumpati, *RSC Adv.* **2013**, *3*, 20471; d) G. Han, C. C. You, B. J. Kim, R. S. Turingan, N. S. Forbes, C. T. Martin, V. M. Rotello, *Angew. Chem., Int. Ed.* **2006**, *45*, 3165.

[21] C. Zhang, Z. Zhou, X. Zhi, Y. Ma, K. Wang, Y. Wang, Y. Zhang, H. Fu, W. Jin, F. Pan, *Theranostics* **2015**, *5*, 134.

[22] Z. Luo, X. Yuan, Y. Yu, Q. Zhang, D. T. Leong, J. Y. Lee, J. Xie, *J. Am. Chem. Soc.* **2012**, *134*, 16662.

[23] a) G. Guan, S. Liu, Y. Cai, M. Low, M. S. Bharathi, S. Zhang, S. Bai, Y.-W. Zhang, M.-Y. Han, *Adv.Mater.* **2014**, *26*, 3427; b) H. Mojzisova, S. Bonneau, C. Vever-Bizet, D. Brault, *Biochim. Biophys. Acta, Biomembr.* **2007**, *1768*, 2748.

[24] Y. Song, W. Shi, W. Chen, X. Li, H. Ma, *J. Mater. Chem.* **2012**, *22*, 12568.

[25] R. Rotomskis, J. Valanciunaite, A. Skripka, S. Steponkiene, G. Spogis, S. Bagdonas, G. Streckyte, *Lith. J. Phys.* **2013**, *53*, 57.

[26] K. Yang, M. Kong, Y. Wei, Y. Liu, X. Cheng, J. Li, H. Park, X. Chen, *J. Mater. Sci.* **2013**, *48*, 1717.

[27] M. Yu, C. Zhou, J. Liu, J. D. Hankins, J. Zheng, *J. Am. Chem. Soc.* **2011**, *133*, 11014.

[28] Y.-H. Moon, S.-M. Kwon, H.-J. Kim, K.-Y. Jung, J.-H. Park, S.-A. Kim, Y.-C. Kim, S.-G. Ahn, J.-H. Yoon, *Oncol. Rep.* **2009**, *22*, 1085.

[29] A. C. E. Moor, *J. Photochem. Photobiol. B* **2000**, *57*, 1.

[30] X. Wang, A. R. Morales, T. Urakami, L. Zhang, M. V. Bondar, M. Komatsu, K. D. Belfield, *Bioconjugate Chem.* **2011**, *22*, 1438.

[31] H. Wang, P. Zhao, X. Liang, X. Gong, T. Song, R. Niu, J. Chang, *Biomaterials* **2010**, *31*, 4129.

[32] H. Chen, B. Li, J. Qiu, J. Li, J. Jin, S. Dai, Y. Ma, Y. Gu, *Nanoscale* **2013**, *5*, 12409.